



Article

Carbonaceous Materials in the Fault Zone of the Longmenshan Fault Belt: 2. Characterization of Fault Gouge from Deep Drilling and Implications for Fault Maturity

Li-Wei Kuo ^{1,*} , Jyh-Rou Huang ², Jiann-Neng Fang ³, Jialiang Si ⁴ , Sheng-Rong Song ⁵, Haibing Li ⁴ and En-Chao Yeh ²

¹ Department of Earth Sciences, National Central University, Taoyuan 320, Taiwan

² Department of Earth Sciences, National Taiwan Normal University, Taipei 106, Taiwan; hjrou0906@hotmail.com (J.-R.H.); ecyeh@ntnu.edu.tw (E.-C.Y.)

³ National Taiwan Museum, Taipei 100, Taiwan; jnfang@ntm.gov.tw

⁴ Institute of Geology, Chinese Academy of Geological Sciences, Beijing 100037, China; gongrenbaqin@126.com (J.S.); lihaibing06@163.com (H.L.)

⁵ Department of Geosciences, National Taiwan University, Taipei 106, Taiwan; srsong@ntu.edu.tw

* Correspondence: liweikuo@ncu.edu.tw; Tel.: +886-3-4227151 (ext. 65628)

Received: 22 June 2018; Accepted: 5 September 2018; Published: 7 September 2018



Abstract: In recent works on the determination of graphitization of carbonaceous materials (CM) within the principal slip zone (PSZ) of the Longmenshan fault (China), we demonstrated that the formation of graphite, resulted from strain and frictional heating, could be evidence of past seismic slip. Here we utilize Raman Spectroscopy of CM (RSCM) on the CM-bearing gouges in the fault zone of the Longmenshan fault belt, at the borehole depth of 760 m (FZ760) from the Wenchuan earthquake Fault Scientific Drilling project-1 (WFSD-1), to quantitatively characterize CM and further retrieve ancient fault deformation information in the active fault. RSCM shows that graphitization of CM is intense in the fault core with respect to the damage zone, with the graphitized carbon resembling those observed on experimentally formed graphite that was frictionally generated. Importantly, compared to the recognized active fault zone of the Longmenshan fault, the RSCM of measured CM-rich gouge shows a higher degree of graphitization, likely derived from high-temperature-perturbation faulting events. It implies that FZ760 accommodated numerous single-event displacement and/or at higher normal stresses and/or in the absence of pore fluid and/or along a more localized slip surface(s). Because graphite is a well-known lubricant, we surmise that the presence of the higher degree graphitized CM within FZ760 will reduce the fault strength and inefficiently accumulate tectonic stress during the seismic cycle at the current depth, and further infer a plausible mechanism for fault propagation at the borehole depth of 590 m during the Mw 7.9 Wenchuan earthquake.

Keywords: graphitization; carbonaceous material; Longmenshan fault; Wenchuan earthquake; WFSD-1

1. Introduction

During an individual seismic event, fault-zone rocks presumably accommodate most of the deformation [1] and likely preserve the evidence of slip events. Deformation events occurring at typical seismic rates of ~1 m/s, considered as localized frictional sliding, may drive thermally activated physical and chemical processes such as flash heating of asperities [2], frictional melting [3], gelification [4], and decarbonation [5]. The products derived from the aforementioned processes have

been experimentally and theoretically demonstrated for fault lubrication during earthquakes [6,7]. In particular, fault pseudotachyrites, derived from rapid solidification of frictional melts, have been naturally and experimentally documented and is widely recognized as the evidence of seismic slip which allows the retrieval of earthquake source parameters [3,8–10]. However, because of severe alteration on fault rocks during long term fluid-rock interaction [11], few other geological evidence of fault slip have been reported [12–16], and it remains challenging to bridge rock record and fault deformation.

The NE–SW-trending active Longmenshan thrust belt, bordering the western margin of the Sichuan basin (China), resulted in the Mw 7.9 Wenchuan earthquake in SE-Tibet and produced a ~240 km-long Yingxiu-Beichuan surface rupture zone (Figure 1a) [17]. Importantly, the Wenchuan earthquake Fault Scientific Drilling project-1 (WFSD-1) was initiated in 2006 to investigate the physical and chemical processes associated with the large slip earthquake, a maximum slip of ~9.5 m and the estimated co-seismic slip velocity up to 3 m/s in Wenchuan [18]. The borehole was drilled to a depth of 1201 m and passed from the Pengguan complex (the hanging wall) into the Xujiahe Formation (the foot wall), approximately remarking the location of the Longmenshan fault zone between 570 m and 595 m at depths (Figure 1b) [19]. The detailed observation of recovered borehole materials indicated that the Longmenshan fault is composed of fault breccias, cataclasites and black fault gouges enriched with poorly crystalline anthracite mainly derived from the coal bed within the Xujiahe Formation [19].

Kuo et al. [20] reported for the first time the co-seismic graphitization occurred within the CM-rich gouge of WFSD-1. As this 54-cm-thick fault gouge hosts the ~200- μ m-thick principal slip zone (PSZ) of the 2008 Mw 7.9 Wenchuan earthquake at the depth of 589.22 m, Kuo et al. [20] proposed that graphitization was likely driven by frictional heating of CM. The discovery of co-seismic graphitization is a potential seismic indicator of fault slip, as graphite is relatively stable at the scale of geological time.

Kuo et al. [21] soon experimentally demonstrated that co-seismic graphitization shows distinguishable characteristics of Raman spectra with respect to the surrounding fault breccia. The rock friction experiments on CM-rich gouge show that CM graphitization results in the variation of peak parameters, presumably due to strain [22] rather than strain rate. In addition, the transformation of poor crystallinity CM into graphite only took place with the presence of high temperature (~300 °C) which was deformed at a seismic rate of 3 m/s under room dry condition. Importantly, Kuo et al. [21] utilized the discovery of graphitization to determine seismic Longmenshan fault movement, which is in accordance with the observation from the WFSD-1 [23,24].

Here we report the first detailed characterization of both CM-bearing gouge and surrounding fault breccia within the Longmenshan fault system recovered from the WFSD-1. The CM-bearing gouge was collected from the borehole depth of ~760 m (Figure 1c). By means of X-ray powder diffraction analysis (XRD) and micro-Raman spectroscopy, we establish a reference minerals and CM data set from the seismically active fault, address the geological evidence of on-fault graphitization, compare the characteristics of graphitization with the recognized active fault zone at 590 m depth (FZ590 hereafter) [19–21], and, by extension, present an application of these data for studies of exhumed CM-bearing fault segments, e.g., the trench at Jiulong where ruptured during the 2008 Mw 7.9 Wenchuan earthquake, as shown in the companion paper.

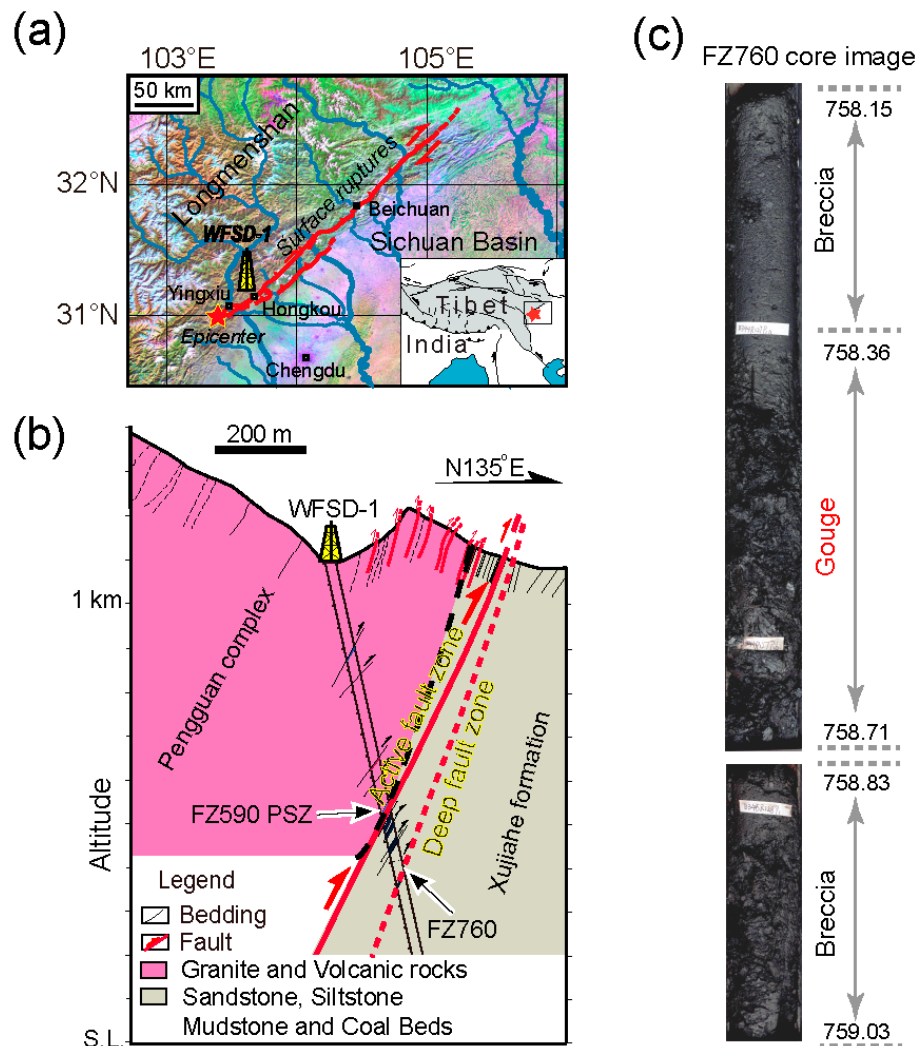


Figure 1. Shaded-relief map of the eastern Tibet showing the major Longmenshan fault belt, the 2008 Mw 7.9 Wenchuan earthquake, China, and the location of the Wenchuan earthquake Fault Scientific Drilling project-1 (WFSD-1) drilling site [19]. (a) The 240 km-long Yingxiu-Beichuan surface rupture and the 80 km-long Guanxian-Anxian surface rupture associated with the Mw 7.9 earthquake, and the location of WFSD-1 site. Red star is the epicenter of the main shock. Inset is a schematic plot of the Tibetan Plateau. (b) An N135°E cross-section of the WFSD-1 showing the Longmenshan fault system and surrounding formations encountered in the borehole. The upper arrow showing the 2008 earthquake principal slip zone located at 589.22 m depth. The lower arrow showing the bottom of the Longmenshan fault system located at 759 m depth (the target fault zone in this study), and the images of core samples of the WFSD-1 was enlarged in the right panel as (c). (c) The core image exhibiting major portions of the FZ760 along the borehole of WFSD-1 including breccia and gouge.

2. Materials and Methods

On the basis of the core description of the WFSD-1, the Longmenshan fault system, made of ten major fault zones, was sandwiched with the Neoproterozoic Pengguan complex (mainly volcanic rocks and pyroclastics) and the Triassic Xujiahe Formation (sandstone, siltstone, and shale with some lamination of coal beds) [19]. Among these, the active Longmenshan fault zone, corresponding to the 2008 Mw 7.9 Wenchuan earthquake, was currently recognized at the depth of 590 m [19], while the bottom of the fault system was reported at the depth of ~760 m (FZ760 hereafter).

Here we utilize the terminology defined by Sibson [25] and Chester et al. [26] for the description of fault architecture and texture. Fault breccias are medium- to coarse-grained incohesive rocks containing

more than 30% visible rock fragments, and fault gouges are clay-rich incohesive rocks with less than 30% visible fragments. In addition, fault gouges are commonly the main constituents within the fault core, while fault breccias are usually made of the damage zone of major faults. Core examination shows that, from top to bottom, the FZ760 contains a sequence of fracture and breccia zone (~5 m width and recognized as the hanging wall damage zone), thick black gouge zone (~35 cm width and recognized as the fault core), fracture and breccia zone (~1 m width and recognized as the foot wall damage zone), and a return to wall rock [19].

In this study we focus on the FZ760 ranged from the depth of 758.15 m to 759.03 m (Figure 1c). We conduct a sequential and continuous collection of fresh samples along the studied depth, except the depth from 758.71 m to 758.83 m because of the core loss during drilling operation. Sixty samples were collected across the FZ760, including sixteen samples of the hanging wall fault breccia (~21 cm), twenty-six samples of the 35 cm-thick black gouge, and another nineteen samples from the footwall fault breccia (~20 cm). Because smeared CMs are likely derived from faulting and preserve the information of fault deformation, we target the clay-size fraction of the samples. All clay-size fraction samples are made by the processes of disaggregation in distilled water, centrifugation, and deposition of draft suspensions of <2 μm on glass slides. We used a PANalytical X'Pert PRO X-ray diffractometer (PANalytical, Almelo, The Netherlands) at National Taiwan University under the conditions of filtered $\text{CuK}\alpha$ (1.540 Å) radiation, 45 kV and 40 mA of X-ray generator, $1.0^\circ \text{min}^{-1}$ scanning speed, and 5° – 40° of 2θ coverage (Figure 2). (Please see the detail in Kuo et al. [27]).

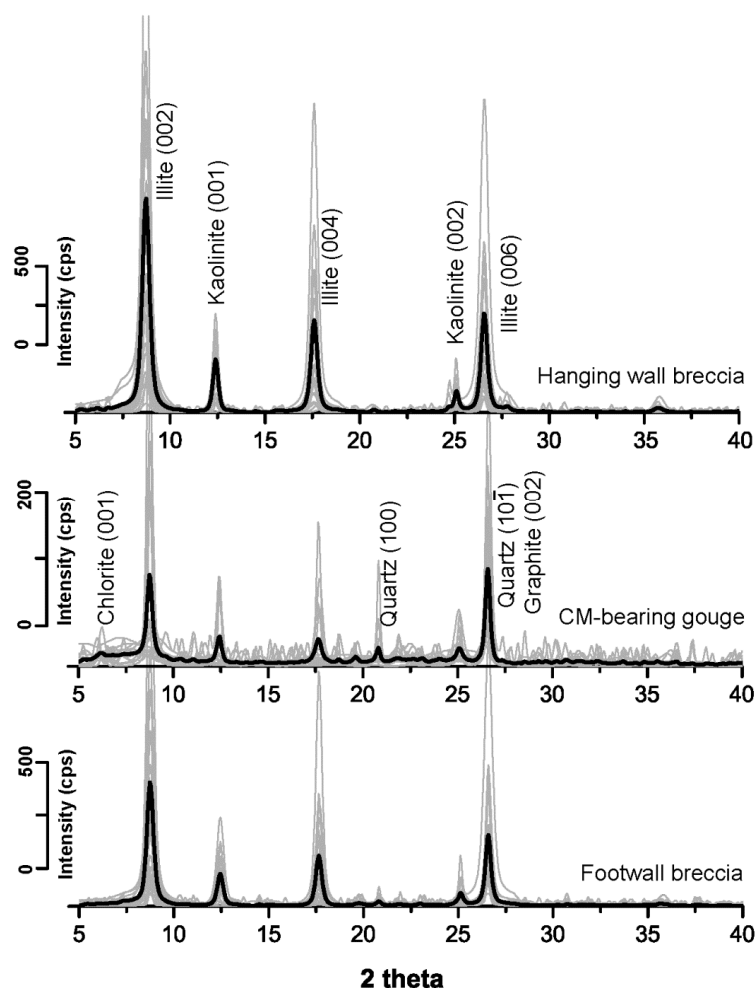


Figure 2. Characterization of mineral phases of FZ760 samples. The mineral phases of breccia are very similar to that of the gouge zone. Comparing the intensity (002) (004) (006) of illite, the XRD data of CM-bearing gouge demonstrated the presence of quartz and graphite. cps, counts per second.

Raman spectroscopy, one of the fastest molecular spectroscopy techniques to determine the configuration of carbon, is recognized as an appropriate tool for the study of CM [28]. We obtained the Raman spectra of CM (RSCM) with an excitation beam of wavelength of 532 nm on the sampled glass slides at room humidity and a laser power of 5 mW without neutral density filters (a Horiba Jobin Yvon UV-VIS Labram HR Micro-Raman spectrometer (HORIBA, Kyoto, Japan) at the National Taiwan Museum), and focused on the 1100–1800 cm^{-1} region of the Raman spectrum which includes all the first-order bands of CM as suggested by Beyssac et al. [29,30]. The first-order bands include the graphite band (from 1575 cm^{-1} to 1592 cm^{-1}) known as the G band and two disorder-induced bands referred to as the “D1 band” (from 1330 cm^{-1} to 1336 cm^{-1}) and “D3 band” (from 1490 cm^{-1} to 1525 cm^{-1}) (Figure 3 inset). We evaluate the relevant parameters of the Raman spectrum (i.e., peak height, peak width, and peak position) by a fitting procedure of the pseudo-Voigt function (Gaussian–Lorentzian linear combination) [31,32]. In addition, two indicative parameters introduced by Kuo et al. [21] were used in this work: (1) The D1/G width ratio versus peak height ratio (Figure 4a), and (2) the D1 and G widths normalized over the average for all samples versus their peak position (Figure 4b). Five measurements per sample were conducted on different sample spots, and each spot was measured with three integration time of 5 s. Mean values are calculated as an average of all the spectral parameters obtained for one single sample. The spectrum of Raman analysis was calibrated with a Si-waver prior to each set of measurement. The curve-fitting in our study is likely influenced by individual operator and might be processed with a standardized curving-fitting procedure as suggested by Lünsdorf [33,34] in the future. Results of spectrum decomposition along the depth are plotted in Figure 5 and summarized in the Table 1.

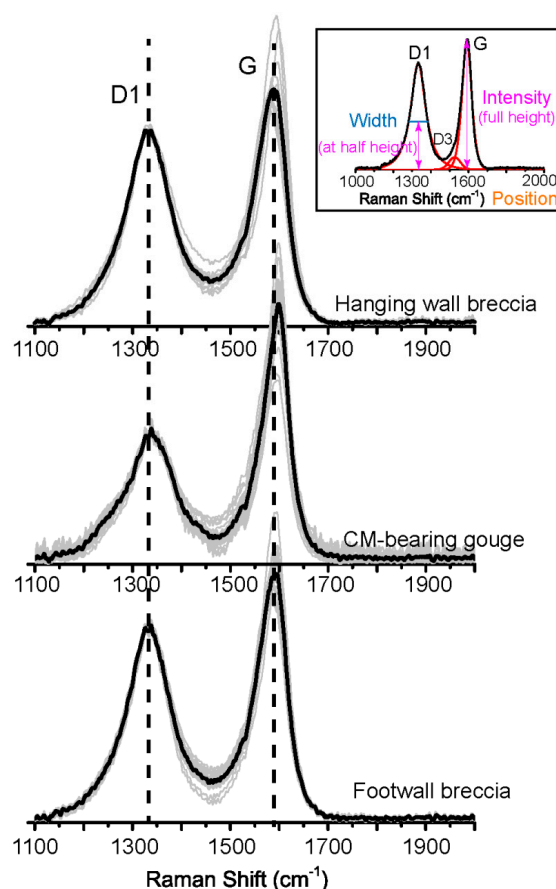


Figure 3. The representative first-order region of Raman spectra from different fault components. The inset shows the usage for defining the indicative parameters derived from the relevant spectrum decomposition (width, intensity, peak position, etc.).

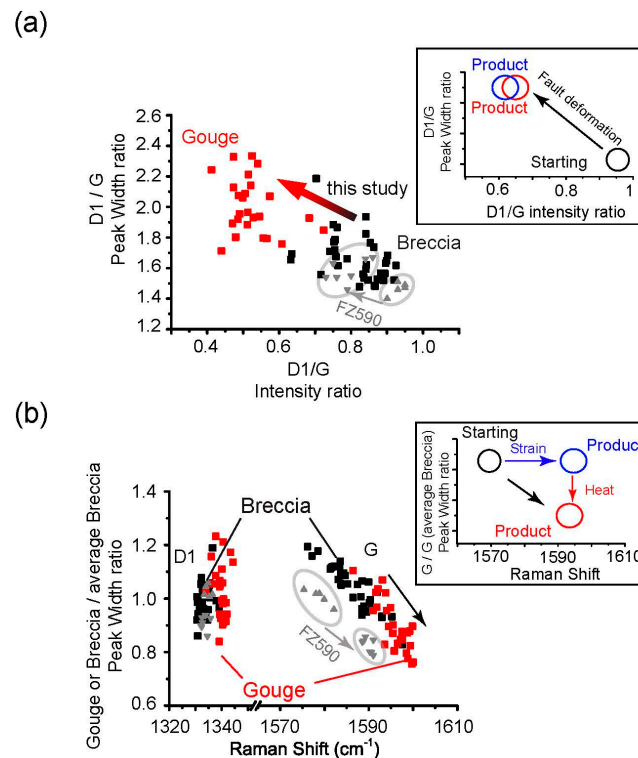


Figure 4. Decomposition of Raman spectra of FZ760 samples. (a) D1/G peak width ratio versus D1/G intensity ratio. Grey triangles representing the FZ590 results, and the grey arrows showing the variation of Raman spectra observed from breccia to gouge [21,33]. The inset showing a representative trend of Raman spectrum derived from the starting materials and deformed gouge [21]. (b) G peak width of gouge over average breccia peak width versus G band peak position. The inset showing a representative trend of Raman spectrum attributing to strain and high temperature pulses derived from the starting materials and deformed gouge [21].

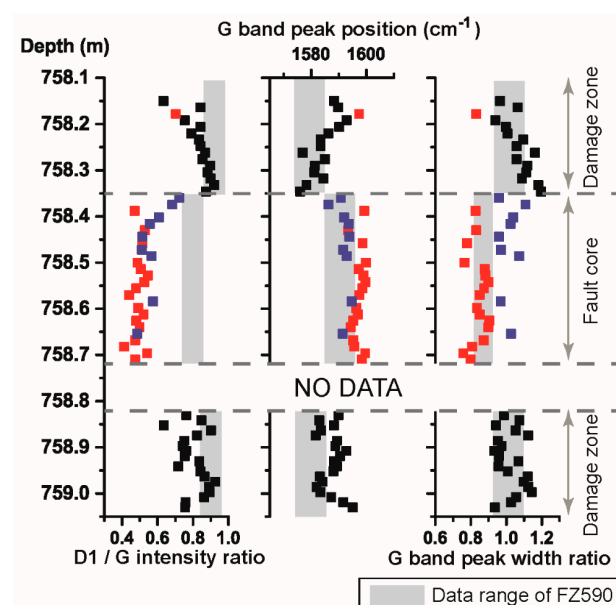


Figure 5. Raman spectra of FZ760 samples across the Longmenshan fault system. Red rectangles indicating the samples containing high R1 value and low G band peak width ratio value with respect to breccia. Blue rectangles indicating the samples containing high R1 value and similar G band peak width ratio value with respect to breccia. Grey rectangles representing the data range of FZ590 by Kuo et al. [21].

Table 1. Spectra decomposition on Raman results of FZ760 from WFSD-1 cores.

Type	Depth (m)	D1/G Intensity (Error Estimate ± 0.07)	D1/G Width Ratio (Error Estimate ± 0.10)	Peak Position (cm^{-1})		Gouge or Breccia/ Average Breccia	
				D1	G	D1	G
Breccia	758.15	0.63	1.66	1334	1588	0.92	0.97
Breccia	758.16	0.84	1.94	1336	1590	1.19	1.06
Breccia	758.18	0.70	2.19	1335	1597	1.05	0.83
Breccia	758.19	0.75	1.77	1334	1593	0.96	0.94
Breccia	758.21	0.84	1.82	1334	1590	1.05	1.00
Breccia	758.22	0.79	1.66	1331	1586	0.97	1.01
Breccia	758.23	0.83	1.56	1330	1583	0.99	1.10
Breccia	758.25	0.84	1.62	1330	1583	0.99	1.06
Breccia	758.26	0.87	1.48	1331	1577	1.00	1.16
Breccia	758.28	0.85	1.77	1332	1585	1.08	1.06
Breccia	758.29	0.90	1.63	1332	1581	1.06	1.12
Breccia	758.30	0.88	1.57	1330	1581	1.01	1.11
Breccia	758.32	0.90	1.65	1333	1584	1.04	1.09
Breccia	758.33	0.92	1.52	1332	1578	1.04	1.18
Breccia	758.35	0.87	1.53	1332	1576	1.06	1.2
Gouge	758.36	0.72	1.85	1334	1591	1.02	0.96
Gouge	758.37	0.68	1.93	1337	1586	1.24	1.11
Gouge	758.39	0.47	1.89	1340	1599	0.90	0.83
Gouge	758.40	0.61	1.76	1339	1592	1.06	1.04
Gouge	758.42	0.56	1.80	1339	1594	1.06	1.02
Gouge	758.43	0.53	1.93	1339	1593	0.93	0.83
Gouge	758.44	0.51	1.97	1337	1594	1.09	0.96
Gouge	758.46	0.51	2.21	1340	1599	1.00	0.78
Gouge	758.47	0.51	1.88	1336	1592	1.06	0.97
Gouge	758.49	0.57	1.79	1340	1593	1.11	1.07
Gouge	758.50	0.49	2.07	1341	1600	0.92	0.76
Gouge	758.51	0.51	2.09	1340	1597	1.06	0.88
Gouge	758.53	0.54	1.94	1341	1599	0.99	0.88
Gouge	758.54	0.52	2.33	1340	1600	1.21	0.90
Gouge	758.56	0.48	1.80	1340	1599	0.91	0.87
Gouge	758.57	0.44	1.71	1339	1597	0.84	0.85
Gouge	758.58	0.57	2.07	1336	1595	1.16	0.97
Gouge	758.60	0.49	1.96	1341	1596	0.94	0.83
Gouge	758.61	0.52	2.14	1339	1597	1.05	0.85
Gouge	758.63	0.48	1.80	1339	1595	0.94	0.90
Gouge	758.64	0.50	2.06	1339	1594	1.07	0.90
Gouge	758.65	0.49	1.92	1344	1591	1.14	1.03
Gouge	758.67	0.47	2.33	1343	1595	1.18	0.87
Gouge	758.68	0.41	2.24	1339	1596	1.05	0.81
Gouge	758.70	0.54	2.28	1340	1600	1.00	0.76
Gouge	758.71	0.47	2.13	1340	1598	0.98	0.80
Breccia	758.83	0.76	1.62	1334	1590	0.92	0.99
Breccia	758.84	0.85	1.52	1331	1583	0.95	1.07
Breccia	758.85	0.63	1.69	1330	1588	0.92	0.94
Breccia	758.86	0.90	1.68	1332	1584	1.03	1.05
Breccia	758.87	0.82	1.48	1332	1582	0.96	1.12
Breccia	758.89	0.75	1.88	1333	1589	0.96	0.97
Breccia	758.91	0.76	1.87	1335	1593	1.01	0.93
Breccia	758.92	0.75	1.72	1333	1590	0.95	0.96
Breccia	758.93	0.84	1.54	1333	1588	0.95	1.07
Breccia	758.94	0.72	1.56	1330	1589	0.86	0.96
Breccia	758.95	0.84	1.59	1333	1588	0.93	1.01
Breccia	758.96	0.86	1.49	1332	1583	0.96	1.12
Breccia	758.97	0.92	1.62	1333	1584	1.03	1.10
Breccia	758.99	0.89	1.52	1332	1582	0.99	1.12
Breccia	759.00	0.89	1.57	1334	1583	1.03	1.14
Breccia	759.01	0.86	1.74	1335	1587	1.06	1.06
Breccia	759.02	0.76	1.68	1337	1592	0.99	1.03
Breccia	759.03	0.75	1.79	1339	1595	0.97	0.93

3. Results

3.1. XRD Analysis

The XRD patterns derived from different fault components (breccia and gouge) are separately plotted (Figure 2). All XRD patterns from an individual fault component (e.g., sixteen samples of the hanging wall fault breccia) are shown in grey color, and its on-average XRD pattern is shown in black color as the representative pattern for the recognition of mineral phases. The common mineral assemblages of $<2\ \mu\text{m}$ within the FZ760 are identified as illite and kaolinite. In particular, the XRD patterns of CM-bearing gouge show the presence of chlorite, quartz, graphite, and high background before $10^\circ\ 2\theta$ coverage likely derived from the presence of illite/smectite mixed-layer minerals, as it is absent in the surrounding breccia zones. It is notable that the presence of numerous tiny peaks in the XRD patterns of CM-bearing gouge shows the complexity of mineral phases (e.g., the groups of feldspar and ferric oxides) within the fault core of FZ760. The occurrence of chlorite and illite/smectite mixed-layer minerals and its formation might provide information of faulting or weathering, as was reported in Kuo et al. [11,27,35], but require systematical microstructural and mineralogical examinations. Further, detailed characterization of clay minerals and other minerals within the studied interval is the subject of ongoing research. Here we just evidence the presence of graphite via XRD analysis because the graphitization of CM and graphite is the main target in this study.

3.2. RSCM

The Raman spectra derived from different fault components (breccia and gouge) are separately plotted (Figure 3). All Raman spectra from an individual fault component (e.g., sixteen samples of the hanging wall fault breccia) are shown in grey color, and the on-average Raman spectrum is shown in black. In addition, the intensities of D1 band were normalized so that D1 band has the same integrated intensity for all spectra, enhancing the variation of integrated intensity of G band and visualizing the differential graphitization of CM. The representative first-order region of Raman spectra of FZ760 shows that D1 band and G band are at around $1335\ \text{cm}^{-1}$ and $1585\ \text{cm}^{-1}$, respectively. In addition, the gouge samples contain larger intensity difference between G band and D1 band than the one of breccia samples. The G band of the gouge samples also occurs at a higher frequency than the one in the breccia samples.

The gouge samples commonly have low values of D1/G intensity ratio and high values of D1/G width ratio with respect to the breccia samples (Figure 4a; Table 1). In addition, most of the gouge samples contains higher frequency of D1 band position ($\sim 1340\ \text{cm}^{-1}$) than breccias samples ($\sim 1330\ \text{cm}^{-1}$), and most of the G band of the gouge has higher frequency and smaller peak width ratio (Figure 4b; Table 1). A summary diagram with the indicative parameters of CM along the depth is shown in Figure 5. Here we group the gouge samples with similar characteristics of Raman parameters; that is, compared to breccia samples, the gouge samples containing high R1 value and low G band peak width ratio are marked in red color, while the others containing high R1 value and similar G band peak width ratio value are shown in blue color. In addition, the reported FZ590 Raman data [21] was also integrated in the Figures 4 and 5 for the discussion of fault maturity.

4. Discussion and Conclusions

Rock friction experiments on CM-rich gouge of WFSD-1 were performed at a normal stress of 8.5 Mpa and at both sub-seismic ($0.0003\ \text{m/s}$) and seismic ($3\ \text{m/s}$) slip rates under room-humidity and water-damped conditions to investigate graphitization of CM [21]. By characterizing the experimentally deformed CM-rich gouge of the WFSD-1, Kuo et al. [21] showed that bulk shear strain was responsible for the G band shifting toward higher frequencies which were observed in both the gouges sheared at sub-seismic and seismic slip rates. Therefore, graphitization of CM was likely attributed to bulk shear strain associated with decreasing D1/G peak intensity ratio plus G band peak position shifting towards

higher frequency. In addition, the rock deformation experiments also demonstrated that graphitization of CM can be facilitated at seismic slip rates under room humidity condition because of transient high temperature pulses and the observation of transformation the CM into graphite [21]. Although the achieved maximum temperature by frictional heating cannot be exactly estimated by the conventionally developed geo-thermometer of RSCM [32], a transient dramatic increase of temperatures on CM presumably grows the graphite which may results in a decrease of G band peak width ratio representing the increasingly crystallized CM. Therefore, the Raman spectra of faulting-relevant graphitization, compared to the surrounding rocks, were characterized with (1) a decrease of D1/G peak intensity ratio plus G band peak position upwards to higher frequency attributed to strain [22,36] which may or may not form graphite and (2) a decrease of G band peak width ratio only observed with the formation of graphite (Figure 4 inset) [21].

The FZ760 samples show similar trends of Raman spectra to Kuo et al. [21], suggesting the CM have experienced fault deformation and triggered faulting-relevant graphitization (Figure 4). Most of gouge samples commonly have low values of D1/G intensity ratio and high values of D1/G width ratio, supporting that fault core accommodated most shear displacement and strain during the seismic cycle (Figure 4a) [25,26]. In addition, the combination of decreasing of G band peak width ratio (Figure 4b) and the presence of graphite (Figure 2) of the gouge zone, evidencing the presence of graphitization of CM triggered by frictional heating, likely illustrate the occurrence of localized, high-velocity seismic slip (e.g., the 2008 Mw 7.9 Wenchuan earthquake) (gouge data marked in red in Figure 5). It is notable that some gouge samples accompanied fault deformation show similar values of G band peak width ratio to the breccia samples (gouge data marked in blue in Figure 5), implying the absence of significant temperature increase but not an indication of aseismic behavior of the faults, because the products from wet experiments at seismic rates show similar characters (e.g., water vaporization buffers temperature rise during co-seismic slip) [21,37]. Interestingly, a few breccia samples show low values of D1/G intensity ratio, G band peak position upwards to higher frequency, and low values of G band peak width (breccia data marked in red in Figure 5). It seems that the breccia samples defined with the grain sizes and visible rock fragments may not be perfectly appropriate because the graphitization of CM or the formation of graphite might be extremely local during seismic faulting (e.g., <300 μm in thickness of the 2008 Mw 7.9 Wenchuan PSZ) and further detailed microstructural and mineralogical examination is required. Our results might provide information and a methodology by which principal slip zones can be recognized in future investigations of active faults.

Because our samples and the samples of FZ590 both showed faulting-relevant graphitization, we may integrate the data (shown in grey in Figure 5) and interpret the variation as follows. In general, FZ760 show the characteristics of RSCM similar to FZ590, except (1) the presence of fault-relevant graphitization characterized with similar values of G band peak width ratio to the breccia samples (Figure 5 shown in blue color), (2) the slightly high frequency (peak position) of gouge samples and breccia samples, and (3) the extremely low values of D1/G intensity ratio. Slip along multiple localized slip surfaces or across a distributed fault network (e.g., [38]), resulted from the multi-fault zone processes (frictional heating and comminution) during earthquakes, seems reasonable for the observation of (1) and (2) because of the heterogeneity of fault zones. However, how the characteristics of RSCM are developed by repeated and different fault deformation (seismic and aseismic slip) remains unknown, and systematic rock friction works on WFSD-1 materials under various conditions are required.

The D1/G intensity ratio is commonly utilized as a gauge to quantify the degree of graphitization [29,30] and is relevant to the parameters including confining pressure, burial time, temperature, fluid, and shear stress/strain [22,29,30,39]. Considering the factors proposed for sedimentary and metamorphic geo-thermometers, the gouge samples of both FZ760 and FZ590 (less than 200 m-thick lithological formation in between) are unlikely to have experienced a significant difference of confining pressure, burial time and thermal gradient temperature resulting in the dramatically variant D1/G intensity ratio between FZ760 (~0.52 on average) and FZ590 (~0.85 on

average). High temperature fluid could have deposited graphitic carbon, as hydrothermal carbon often exhibits higher crystallinity [40,41]. In addition, the temperature profile of the WFSD-1 showed a broad zone (from 625 m to 755 m in depth) of high temperature anomaly [24,42], implying the presence of a potential conduit for transporting hydrothermal fluid. However, the fracture densities calculated from WFSD-1 core observation [19] are in good agreement with the abnormal thermal anomalies in the depth interval between 625 m and 755 m. It indicates fluid flows in the fracture zones [42] and suggests the deposition of graphite will be pervasive in the fracture zones (or damage zones) instead of low-permeability gouge zone. The integration of our high D1/G intensity ratio of breccia samples (Figure 4a) plus no known deposited graphite veins associated with the WFSD-1 cores [19] suggests that graphite within FZ760 gouge zone is unlikely to have formed by the deposition of hydrothermal fluid. The identification of the origin of graphite within FZ760 remains challenging because Raman spectroscopy is not sufficient to detail the nanostructures of CM, which should be integrated with transmission electron microscope imaging and geochemical analyses in the future.

Finally, shear strain seems to be the potentially dominant parameter for the significant decrease of FZ760 D1/G intensity ratio with respect to FZ590. Rock deformation experiments demonstrated that strain can facilitate the transformation of sp^3 (diamond-like) clusters into sp^2 (graphite-like) clusters [21,22] which is inversely proportional to the D1/G intensity ratio [36]. It likely suggests that FZ760 experienced major accumulated strain in the past and was a mature fault with respect to the FZ590 (Figure 5). Importantly, phase transformation from CM to graphite was found in both FZ760 and FZ590, and the presence of graphite can reduce the fault strength [43] (Figures 2 and 4). The numerous re-hybridization of sp^3 to sp^2 was proposed to form the lubricious amorphous sp^2 -containing carbon (e.g., [44]), and it seems likely that the presence of widely distributed sp^2 -containing carbon (even not graphite) may additionally increase lubricity and result in fault strength reduction. Since graphite is a well-known lubricant, the FZ760, hosting the enrichment of graphite and lubricious amorphous sp^2 -containing carbon as a weak fault zone, is suggested to inefficiently accumulate tectonic stress during the seismic cycle. In addition, graphite enrichment results in fault-zone weakness where it forms a continuous weak layer, thereby promoting fault creep and/or inhibiting the accumulation of stored elastic strain energy. However, the along-strike and down-dip extent of graphite enrichment remains the focus of future research.

Author Contributions: L.-W.K. wrote the paper and coordinated the study; L.-W.K. conceived the present idea and planned the experiments; J.-R.H. conducted the experiments; L.-W.K. and J.-R.H. analyzed the data; J.-N.F., J.S., S.-R.S. and H.L. contributed materials and analysis tools; E.-C.Y. took part to the discussion.

Funding: This work was partially supported by the National Science Foundation of China (41572192, 41330211, 41520104006) to Haibing Li, and mainly by the Taiwan ROC (Republic of China) Ministry of Science and Technology (MOST 105-2628-M-008-002-MY3) and NCU grants to Li-Wei Kuo.

Acknowledgments: We thank two anonymous reviewers, and the Editor Chen for their positive and constructive comments. This research used materials provided by the “WFSD” of the National Science and Technology Planning Project.

Conflicts of Interest: The authors declare no conflict of interest.

References

1. Sibson, R.H. Thickness of the seismic slip zone. *Seismol. Soc.* **2003**, *93*, 1169–1178. [[CrossRef](#)]
2. Goldsby, D.L.; Tullis, T.E. Low frictional strength of quartz rocks at subseismic slip rates. *Geophys. Res. Lett.* **2002**, *29*, 1844. [[CrossRef](#)]
3. Di Toro, G.; Hirose, T.; Nielsen, S.; Pennacchioni, G.; Shimamoto, T. Natural and experimental evidence of melt lubrication of faults during earthquakes. *Science* **2006**, *311*, 647–649. [[CrossRef](#)] [[PubMed](#)]
4. Di Toro, G.; Goldsby, D.L.; Tullis, T.E. Friction falls towards zero in quartz rock as slip velocity approaches seismic rates. *Nature* **2004**, *427*, 436–439. [[CrossRef](#)] [[PubMed](#)]
5. Han, R.; Shimamoto, T.; Hirose, T.; Ree, J.-H.; Ando, J. Ultralow friction of carbonate faults caused by thermal decomposition. *Science* **2007**, *316*, 878–881. [[CrossRef](#)] [[PubMed](#)]

6. Di Toro, G.; Han, R.; Hirose, T.; De Paola, N.; Nielsen, S.; Mizoguchi, K.; Ferri, F.; Cocco, M.; Shimamoto, T. Fault lubrication during earthquakes. *Nature* **2011**, *471*, 494–498. [[CrossRef](#)] [[PubMed](#)]
7. Niemeijer, A.; Di Toro, G.; Griffith, W.A.; Bistacchi, A.; Smith, S.A.F.; Nielsen, S. Inferring earthquake physics and chemistry using an integrated field and laboratory approach. *J. Struct. Geol.* **2012**, *39*, 2–36. [[CrossRef](#)]
8. Sibson, R.H. Generation of pseudotachylite by ancient seismic faulting. *Geophys. J. R. Astron. Soc.* **1975**, *43*, 775–794. [[CrossRef](#)]
9. Tsutsumi, A.; Shimamoto, T. High-velocity frictional properties of gabbro. *Geophys. Res. Lett.* **1997**, *24*, 699–702. [[CrossRef](#)]
10. Di Toro, G.; Pennacchioni, G.; Nielsen, S.; Eiichi, F. Pseudotachylites and earthquake source mechanics. In *International Geophysics*; Fukuyama, E., Ed.; Academic Press: Cambridge, MA, USA, 2009; Volume 94, pp. 87–133.
11. Kuo, L.-W.; Song, S.-R.; Yeh, E.C.; Chen, H.F.; Si, J. Clay mineralogy and geochemistry investigations in the host rocks of the Chelungpu fault, Taiwan: Implication for faulting mechanism. *J. Asian Earth Sci.* **2012**, *59*, 208–218. [[CrossRef](#)]
12. Rowe, C.D.; Fagereng, A.; Miller, J.A.; Mapani, B. Signature of coseismic decarbonation in dolomitic fault rocks of the Naukluft Thrust, Namibia. *Earth Planet. Sci. Lett.* **2012**, *333–334*, 200–210. [[CrossRef](#)]
13. Kirkpatrick, J.D.; Rowe, C.D.; White, J.C.; Brodsky, E.E. Silica gel formation during fault slip: Evidence from the rock record. *Geology* **2013**, *41*, 1015–1018. [[CrossRef](#)]
14. Smith, S.A.F.; Di Toro, G.; Kim, S.; Ree, J.-H.; Nielsen, S.; Billi, A.; Spiess, R. Coseismic recrystallization during shallow earthquake slip. *Geology* **2013**, *41*, 63–66. [[CrossRef](#)]
15. Evans, J.P.; Prante, M.R.; Janecke, S.U.; Ault, A.K.; Newell, D. Hot faults: Iridescent slip surfaces with metallic luster document high-temperature ancient seismicity in the Wasatch fault zone, Utah, USA. *Geology* **2014**, *42*, 623–626. [[CrossRef](#)]
16. Kuo, L.-W.; Song, S.-R.; Suppe, J.; Yeh, E.C. Fault mirrors in seismically active fault zones: A fossil of small earthquakes at shallow depths. *Geophys. Res. Lett.* **2016**, *43*, 1950–1959. [[CrossRef](#)]
17. Xu, X.; Wen, W.; Yu, G.; Klinger, Y.; Hubbard, J.; Shaw, J. Coseismic reverse- and oblique-slip surface faulting generated by the 2008 Mw 7.9 Wenchuan earthquake, China. *Geology* **2009**, *37*, 515–518. [[CrossRef](#)]
18. Xu, C.; Liu, Y.; Wen, Y.; Wang, R. Coseismic slip distribution of the 2008 Mw 7.9 Wenchuan earthquake from Joint Inversion of GPS and InSAR data. *Seismol. Soc.* **2010**, *100*, 2736–2749. [[CrossRef](#)]
19. Li, H.; Wang, H.; Xu, Z.; Si, J.; Pei, J.; Li, T.; Huang, Y.; Song, S.-R.; Kuo, L.-W.; Sun, Z.; et al. Characteristics of the fault-related rocks, fault zones and the principal slip zone in the Wenchuan earthquake Fault Scientific Drilling Hole-1 (WFSD-1). *Tectonophysics* **2013**, *584*, 23–42. [[CrossRef](#)]
20. Kuo, L.-W.; Li, H.; Smith, S.A.F.; Di Toro, G.; Suppe, J.; Song, S.-R.; Nielsen, S.; Sheu, H.-S.; Si, J. Gouge graphitization and dynamic fault weakening during the 2008 Mw 7.9 Wenchuan earthquake. *Geology* **2014**, *42*, 47–50. [[CrossRef](#)]
21. Kuo, L.-W.; Di Felice, F.; Spagnuolo, E.; Di Toro, G.; Song, S.-R.; Aretusini, S.; Li, H.; Suppe, J.; Si, J.; Wen, C.-Y. Fault gouge graphitization as evidence of past seismic slip. *Geology* **2017**, *45*, 979–982. [[CrossRef](#)]
22. Ross, J.V.; Bustin, R.M. The role of strain energy in creep graphitization of anthracite. *Nature* **1990**, *343*, 58–60. [[CrossRef](#)]
23. Si, J.; Li, H.; Kuo, L.-W.; Pei, J.; Song, S.-R.; Wang, H. Clay mineral anomalies in the Yingxiu-Beichuan fault zone from the WFSD-1 drilling core and its implication for the faulting mechanism during the 2008 Wenchuan earthquake (Mw 7.9). *Tectonophysics* **2014**, *619–620*, 171–178. [[CrossRef](#)]
24. Li, H.; Xue, L.; Brodsky, E.E.; Mori, J.J.; Fulton, R.M.; Wang, H.; Kano, Y.; Yun, K.; Harris, R.N.; Gong, Z.; et al. Long-term temperature records following the Mw 7.9 Wenchuan (China) earthquake are consistent with low friction. *Geology* **2015**, *43*, 163–166. [[CrossRef](#)]
25. Sibson, R.H. Fault rocks and fault mechanisms. *J. Geol. Soc. Lond.* **1977**, *133*, 191–213. [[CrossRef](#)]
26. Chester, F.M.; Evans, J.P.; Biegel, R.L. Internal structure and weakening mechanisms of the San Andreas fault. *J. Geophys. Res.* **1993**, *98*, 771–786. [[CrossRef](#)]
27. Kuo, L.-W.; Song, S.-R.; Huang, L.; Yeh, E.C.; Chen, H.F. Temperature estimates of coseismic heating in clay-rich fault gouges, the Chelungpu fault zone, Taiwan. *Tectonophysics* **2011**, *502*, 315–327. [[CrossRef](#)]
28. Wopenka, B.; Pasteris, J.D. Structural characterization of kerogens to granulite-facies graphite: Applicability of Raman microprobe spectroscopy. *Am. Mineral.* **1993**, *78*, 533–557.

29. Beyssac, O.; Rouzaud, J.N.; Goffé, B.; Brunet, F.; Chopin, C. Graphitization in a high-pressure, low-temperature metamorphic gradient: A Raman microspectroscopy and HRTEM study. *Contrib. Mineral. Petrol.* **2002**, *143*, 19–31. [[CrossRef](#)]
30. Beyssac, O.; Goffé, B.; Petit, J.P.; Froigneux, E.; Moreau, M.; Rouzaud, J.N. On the characterization of disordered and heterogeneous carbonaceous materials by Raman spectroscopy. *Spectrochim. Acta Part A* **2003**, *59*, 2267–2276. [[CrossRef](#)]
31. Sadezky, A.; Muckenhuber, H.; Grothe, H.; Niessner, R.; Poschl, U. Raman microspectroscopy of soot and related carbonaceous materials: Spectral analysis and structural information. *Carbon* **2005**, *43*, 1731–1742. [[CrossRef](#)]
32. Furuichi, H.; Ujiie, K.; Kouketsu, Y.; Saito, T.; Tsutsumi, A.; Wallis, S. Vitrinite reflectance and Raman spectra of carbonaceous material as indicators of frictional heating on faults: Constraints from friction experiments. *Earth Planet. Sci. Lett.* **2015**, *424*, 191–200. [[CrossRef](#)]
33. Lunsdorf, N.K.; Dunkl, I.; Schmidt, B.; Rantitsch, G.; von Eynatten, H. Towards a higher comparability of geothermometric data obtained by Raman spectroscopy of carbonaceous material. Part 1: Evaluation of biasing factors. *Geostand. Geoanal. Res.* **2014**, *38*, 73–94. [[CrossRef](#)]
34. Lunsdorf, N.K.; Dunkl, I.; Schmidt, B.; Rantitsch, G.; von Eynatten, H. Towards a higher comparability of geothermometric data obtained by Raman spectroscopy of carbonaceous material. Part 2: A revised geothermometer. *Geostand. Geoanal. Res.* **2017**, *41*, 593–612. [[CrossRef](#)]
35. Kuo, L.-W.; Song, S.-R.; Yeh, E.-C.; Chen, H.-F. Clay mineral anomalies in the fault zone of the Chelungpu Fault, Taiwan, and their implications. *Geophys. Res. Lett.* **2009**, *36*, L18306. [[CrossRef](#)]
36. Ferrari, A.C.; Robertson, J. Interpretation of Raman spectra of disordered and amorphous carbon. *Phys. Rev.* **2000**, *61*, 14095–14107. [[CrossRef](#)]
37. Chen, J.; Niemeijer, A.; Yao, L.; Ma, S. Water vaporization promotes coseismic fluid pressurization and buffers temperature rise. *Geophys. Res. Lett.* **2017**, *44*, 2177–2185. [[CrossRef](#)]
38. Faulkner, D.R.; Lewis, A.C.; Rutter, E.H. On the internal structure and mechanics of large strike-slip fault zones: Field observations of the Carboneras fault in southeastern Spain. *Tectonophysics* **2003**, *367*, 235–251. [[CrossRef](#)]
39. Rouzaud, J.-N.; Oberlin, A. Structure, microtexture, and optical properties of anthracene and saccharose-based carbons. *Carbon* **1989**, *27*, 517–529. [[CrossRef](#)]
40. Rumble, D. Hydrothermal graphitic carbon. *Element* **2014**, *10*, 427–433. [[CrossRef](#)]
41. Galvez, M.E.; Beyssac, O.; Martinez, I.; Benzerara, K.; Chaduteau, C.; Malvoisin, B.; Malavieille, J. Graphite formation by carbonate reduction during subduction. *Nat. Geosci.* **2013**, *6*, 473–477. [[CrossRef](#)]
42. Zheng, Y.; Li, H.; Gong, Z. Geothermal study at the Wenchuan earthquake Fault Scientific Drilling project-hole 1 (WFSD-1): Borehole temperature, thermal conductivity, and well log data. *J. Asian Earth Sci.* **2016**, *117*, 23–32. [[CrossRef](#)]
43. Oohashi, K.; Hirose, T.; Shimamoto, T. Graphite as a lubricating agent in fault zones: An insight from low- to high-velocity friction experiments on a mixed graphite-quartz gouge. *J. Geophys. Res.* **2013**, *118*, 2067–2084. [[CrossRef](#)]
44. Erdemir, A.; Donnet, C. Tribology of diamond-like carbon films: Recent progress and future prospects. *J. Phys. D Appl. Phys.* **2006**, *39*, 311–327. [[CrossRef](#)]

